A two-layer granular landslide model for tsunami wave generation: Theory and computation

Gangfeng Ma [a,*], James T. Kirby [b], Tian-Jian Hsu [b], Fengyan Shi [b]

[a] *Department of Civil and Environmental Engineering, Old Dominion University, Norfolk, VA 23529 USA*
[b] *Center for Applied Coastal Research, Department of Civil and Environmental Engineering, University of Delaware, Newark DE 19716 USA*

A R T I C L E   I N F O

A B S T R A C T

We develop and test a new two-layer model for granular landslide motion and tsunami wave generation. The landslide is described as a saturated granular flow, accounting for intergranular stresses governed by Coulomb friction. Tsunami wave generation is simulated by the three-dimensional non-hydrostatic wave model NHWAVE, which is capable of capturing wave dispersion efficiently using a small number of discretized vertical levels. Depth-averaged governing equations for the granular landslide are derived in a slope-oriented coordinate system, taking into account the dynamic interaction between the lower-layer granular landslide and upper-layer water motion. The model is tested against an analytical solution for granular dam-break flow and 2D and 3D laboratory experiments on impulsive wave generation by subaerial granular landslides. Model results illustrate a complex interplay between the granular landslide and tsunami waves, and they reasonably predict not only the tsunami wave generation but also the granular landslide motion from initiation to deposition.

© 2015 Elsevier Ltd. All rights reserved.

1. Introduction

Tsunamis can be generated by subaerial or submarine landslides in reservoirs, lakes, fjords, bays and oceans. Examples include tsunamis generated by subaerial landslides in Lituya Bay, Alaska in 1958 (Fritz et al., 2001, 2009; Weiss et al., 2009), Puerto Aysen, Chile in 2007 (Naranjo et al., 2009; Sepulveda and Serey, 2009), Tafjord, Norway in 1934 (Braathen et al., 2004; Harbitz et al., 1993), and by submarine landslides at Grand Banks, Newfoundland in 1929 (Fine et al., 2005), Papua New Guinea in 1998 (Synolakis et al., 2002; Tappin et al., 2001, 2002), Haiti in 2010 (Fritz et al., 2012) and Japan in 2011 (Tappin et al., 2014). The potential role played by large scale SMF's in tsunami climatology has been reviewed recently by Masson et al. (2006) and Harbitz et al. (2014). Compared to seismogenic tsunamis, landslide or submarine mass failure (SMF) tsunamis are normally characterized by relatively shorter wave lengths and stronger wave dispersion, and potentially may generate large wave amplitudes locally and high run-up along adjacent coastlines. Due to a complex interplay between the landslide and tsunami waves, accurate simulation of landslide motion as well as tsunami generation is a challenging task.

The development of models for landslide tsunami generation centers around two main focuses: choice of a physical model for landslide rheology, and choice of a level of approximation of the flow field and pressure field in the hydrodynamic model used to simulate the generation and propagation of resulting waves. The developer must also decide on the details of interaction between kinematics and dynamics of the landslide material and overlying water column. The hydrodynamics of landslide-induced tsunamis has been extensively studied using numerical models based on different levels of simplification. Examples, in increasing order of completeness in the underlying theory, include shallow water equations (Fine et al., 2005; Harbitz, 1992; Jiang and Leblond, 1992, 1993), Boussinesq equations (Fuhrman and Madsen, 2009; Lynett and Liu, 2003; Watts et al., 2003; Zhou and Teng, 2010), 3D non-hydrostatic models (Ma et al., 2013; 2012), fully nonlinear potential flow theory (Grilli et al., 2002; Grilli and Watts, 1999, 2005) and Navier–Stokes equations (Abadie et al., 2010; Ataie-Ashtiani and Shobeyri, 2008; Heinrich, 1992; Horrillo et al., 2013; Liu et al., 2005; Lovholt et al., 2008; Mader, 2004; Montagna et al., 2011; Quecedo et al., 2004; Yuk et al., 2006). Each of these approaches can provide useful information in suitable parameter ranges; however, full Navier–Stokes solvers are still numerically demanding. In the development below, we concentrate on further extensions to the non-hydrostatic modeling approach.

Most models of landslide or SMF tsunami generation consider the landslides as rigid blocks with prescribed landslide shape and behavior. Landslide motion is specified based on laboratory

* Corresponding author. Tel.: +1 757 683 4732; fax: +302 2563163.
E-mail address: gma@odu.edu (G. Ma).

measurements or on an equation of motion based on the balance of forces acting on the sliding mass, including weight, buoyancy, friction, hydrodynamic drag and inertia forces (Enet and Grilli, 2007). This approach has been widely employed for estimating tsunami hazard (Grilli et al., 2015; Tappin et al., 2014). As discussed by Abadie et al., (2012, 2010), however, this methodology has severe limitations in application to real cases, where landslides may be deformable and have time-varying 3D geometry.

Another approach to simulating landslide-induced tsunamis is to consider both the landslide and the water as two different fluids. This approach allows the landslide to deform, and is capable of describing the two-way coupling between the landslide and surrounding water. Tremendous effort has been devoted to developing this type of model. For example, Jiang and Leblond (1992, 1993) developed a two-layer model in which the lower-layer landslide was treated as either a laminar incompressible viscous fluid or a Bingham visco-plastic fluid, with the deformable underwater landslide and associated tsunami waves dynamically coupled. This approach has been further developed by Fine et al. (2005) and Skvortsov and Bornhold (2007). Abadie et al. (2012) employed a 3D multi-fluid Navier–Stokes model THETIS to simulate tsunami waves generated by the potential collapse of the west flank of the Cumbre Vieja Volcano (CVV), Canary Islands, Spain. The landslide and water were considered as two immiscible fluids with different densities. The free surface as well as the landslide-water interface were captured using a volume of fluid (VOF) algorithm. A similar approach is employed by Horrillo et al. (2013). Assier-Rzadkiewicz et al. (1997) modeled the underwater landslide as sediment-water mixture, with rheology varying from linear fluid viscosity at low sediment concentration to Bingham visco-plastic rheology at high concentration. The model was applied to simulate a laboratory landslide and could reproduce the water waves generated by the landslide with reasonable accuracy. Heinrich et al. (1998) implemented the same approach in a 3D Navier–Stokes solver, and applied the model to study water waves generated by a potential debris avalanche in Montserrat, Lesser Antilles. This approach was also adopted and implemented by Ma et al. (2013) in the non-hydrostatic wave model NHWAVE, without inclusion of the Bingham visco-plastic behavior at high concentration. Their model was not able to capture landslide deposition.

The two-fluid models described above can be reasonably successful in predicting tsunami wave generation. However, they often fail to correctly simulate landslide motion from initiation to deposition. Underwater landslides are gravity-driven flows of dense grain-fluid mixture. Fluid or visco-plastic continuum rheologies typically are not sufficient to explain details of landslide behavior, from initiation of motion from a quasi-equilibrium initial static state, through dynamics of the evolving slide, to final arrest of motion and landslide deposition (Iverson and George, 2014). It is necessary to consider the intergranular stresses and pore fluid pressure in the landslide model. Initial steps towards development of granular flow-based models for landslide behavior have usually been based on depth-integrated models pioneered by Iverson (1997); Savage and Hutter (1989) and others. These models were initially developed for application to shallow subaerial debris flows. Pioneering work to implement these formulations as models for submarine landslides were carried out by Kelfoun et al. (2010) and Giachetti et al. (2011), among others. In their model, the landslide was simulated by a depth-averaged granular flow model, in which the intergranular stresses were modeled by Coulomb friction. Tsunami wave generation was simulated using a shallow-water equation model based on the assumption that the landslide-induced tsunamis are long waves, as in the previous two-fluid models of Jiang and Leblond (1992, 1993), Fine et al. (2005) and Skvortsov and Bornhold (2007). The model was used to examine the consistency of run-up predictions with patterns of sediment deposition which are hypothesized to be the result of tsunami inundation. Their model,

however, contains several critical limitations. The Coulomb frictional retarding stress was assumed to be constant over the whole domain. Wave dispersion was not captured due to the shallow-water assumption.

In this paper, we establish a numerical model for the generation and propagation of tsunami waves by granular landslides. A discrete two-layer landslide-induced tsunami generation model is developed and validated using analytical solutions and laboratory measurements. The landslide is described as a granular flow accounting for intergranular stresses governed by Coulomb friction, following the theoretical framework described by Savage and Hutter (1989) and Iverson (1997). Tsunami wave generation is simulated using the 3D non-hydrostatic wave model NHWAVE, which is fully nonlinear and is capable of efficiently capturing wave dispersion using 3–5 discretized vertical levels and simulating wave breaking and associated wave energy dissipation by a shock-capturing scheme. The governing equations for the granular landslide and tsunami waves are coupled dynamically and solved using a Godunov-type finite volume TVD scheme.

The remainder of the paper is organized as follows. Section 2 presents the theoretical basis for the two-layer granular landslide and tsunami wave model. The formulation for the lower-layer granular landslide is derived. The interactions between the landslide and surrounding water as well as the numerical schemes employed to solve the granular flow equations are also discussed. The granular landslide model is first validated in Section 3 using an analytical solution for dam-break flow developed by Mangeney et al. (2000). The model is then applied to study waves generated by a 2D granular landslide in Section 4 and a 3D granular landslide in Section 5. Conclusions and avenues of future model improvement are presented in Section 6.

2. Two-layer Granular landslide and tsunami model

In this section, we derive the formulations for the two-layer granular landslide and tsunami model. In this model, the landslide motion and tsunami wave generation are simulated by separate model components. The lower-layer landslide movement is simulated by a granular flow model, while the upper-layer tsunami wave motion is simulated by the three-dimensional Non-Hydrostatic WAVE model NHWAVE (Ma et al., 2012). The lower layer landslide and upper layer water interact at each time step, maintaining a fully-coupled kinematic and dynamic connection between the layers.

2.1. Lower-layer granular landslide

In this study, we simulate the landslide as a saturated granular debris flow. The details of the derivation follow from Iverson and Denlinger (2001) unless otherwise noted. Following Iverson (1997) and Iverson and Denlinger (2001), we adopt a slope-oriented coordinate system as shown in Fig. 1, with x' oriented down-slope, y' along slope and z' oriented upwards and perpendicular to the slope. Mass and momentum conservation equations from continuum mixture theory are given by

$$\nabla' \cdot \mathbf{v} = 0 \tag{1}$$

$$\rho \left(\frac{\partial \mathbf{v}}{\partial t} + \mathbf{v} \cdot \nabla' \mathbf{v} \right) = -\nabla' \cdot \mathbf{T} + \rho \mathbf{g} \tag{2}$$

Here, $\rho = \rho_s \gamma_s + \rho_f \gamma_f$ is mixture density, ρ_s and ρ_f are the densities of solid and fluid, respectively, and γ_s and γ_f are volume fractions of solid and fluid, respectively. $\mathbf{v} = (v_{x'}, v_{y'}, v_{z'})$ is the mixture velocity, given by $\mathbf{v} = (\rho_s \gamma_s \mathbf{v}_s + \rho_f \gamma_f \mathbf{v}_f)/\rho$, with $\mathbf{v}_s$ and $\mathbf{v}_f$ being the velocities for solid and fluid phases. $\mathbf{T} = \mathbf{T}_s + \mathbf{T}_f$ is the total stress tensor for the mixture and consists of contributions from the fluid and solid

phases, with **T** defined as positive in compression. $\mathbf{g} = (g_{x'}, g_{y'}, g_{z'})$ is the gravitational acceleration vector.

Further simplifications of the governing equations can be achieved by assuming the characteristic horizontal length scale l of the landslide is much greater than the characteristic vertical length scale h (i.e. $h/l \ll 1$), which is usually true in landslides. Based on scaling analysis, the acceleration and horizontal diffusion terms in the vertical momentum equation are at least an order of magnitude smaller than the gravitational acceleration and vertical diffusion terms, thus the equation can be reduced to

$$\rho g_{z'} = -\frac{\partial T^s_{z'z'}}{\partial z'} - \frac{\partial T^f_{z'z'}}{\partial z'} = -\frac{\partial T^s_{z'z'}}{\partial z'} - \frac{\partial P^f}{\partial z'} \tag{3}$$

where $T^s_{z'z'}$ and $T^f_{z'z'}$ are normal stresses in the solid and fluid phase, respectively. P^f is the pressure in the fluid phase. At the landslide-water interface, we have $P^f|_{z'=h_a} = P^f_h$, with $h_a(x', y', t)$ being the local time-varying thickness of the landslide. The solid stress should vanish at the landslide-water interface, so that $T^s_{z'z'}|_{z'=h_a} = 0$.

Integrating Eq. (3) from 0 to h_a and using the boundary condition for $T^s_{z'z'}$ at the interface $z' = h_a$, we get

$$T^s_{z'z'b} = T^s_{z'z'}(x', y', 0) = \rho g_{z'} h_a + P^f_h - P^f_b \tag{4}$$

where subscript b refers to the bed. We assume that fluid pressure inside the landslide varies linearly with depth. Thus, the pore pressure at the bed is given by

$$P^f_b = P^f_h + \lambda \rho g_{z'} h_a \tag{5}$$

where λ is a parameter to be determined. In granular flow, the pore pressure varies temporally and spatially, and has to be obtained by solving an additional equation. Here, we simply assume λ is a constant which will be calibrated using laboratory measurements.

Substituting Eqs. (5) into (4), we obtain the z' direction normal stress $T^s_{z'z'}$ at the bed,

$$T^s_{z'z'b} = (1 - \lambda) \rho g_{z'} h_a \tag{6}$$

and the depth-averaged z' direction normal stress,

$$\overline{T}^s_{z'z'} = \frac{1}{2}(1 - \lambda) \rho g_{z'} h_a \tag{7}$$

A depth-integrated model for landslide motion is next obtained by integrating Eqs. (1) and (2) over the landslide thickness. The depth-averaged mass and momentum equations in the x' and y' directions are given by

$$\frac{\partial h_a}{\partial t} + \frac{\partial (h_a u_a)}{\partial x'} + \frac{\partial (h_a v_a)}{\partial y'} = 0 \tag{8}$$

$$\rho \left[\frac{\partial (h_a u_a)}{\partial t} + \frac{\partial (h_a u_a^2)}{\partial x'} + \frac{\partial (h_a u_a v_a)}{\partial y'} \right]$$
$$= \rho g_{x'} h_a - \int_0^{h_a} \left[\frac{\partial T^s_{x'x'}}{\partial x'} + \frac{\partial T^f_{x'x'}}{\partial x'} \right.$$
$$\left. + \frac{\partial T^s_{y'x'}}{\partial y'} + \frac{\partial T^f_{y'x'}}{\partial y'} + \frac{\partial T^s_{z'x'}}{\partial z'} + \frac{\partial T^f_{z'x'}}{\partial z'} \right] dz' \tag{9}$$

$$\rho \left[\frac{\partial (h_a v_a)}{\partial t} + \frac{\partial (h_a u_a v_a)}{\partial x'} + \frac{\partial (h_a v_a^2)}{\partial y'} \right]$$
$$= \rho g_{y'} h_a - \int_0^{h_a} \left[\frac{\partial T^s_{x'y'}}{\partial x'} + \frac{\partial T^f_{x'y'}}{\partial x'} \right.$$
$$\left. + \frac{\partial T^s_{y'y'}}{\partial y'} + \frac{\partial T^f_{y'y'}}{\partial y'} + \frac{\partial T^s_{z'y'}}{\partial z'} + \frac{\partial T^f_{z'y'}}{\partial z'} \right] dz' \tag{10}$$

where u_a and v_a are depth-averaged velocities in x' and y' directions, respectively.

2.1.1. Evaluation of solid stresses

The depth-averaged solid stresses in the x' direction momentum equation may be approximated by

$$-\int_0^{h_a} \left[\frac{\partial T^s_{x'x'}}{\partial x'} + \frac{\partial T^s_{y'x'}}{\partial y'} + \frac{\partial T^s_{z'x'}}{\partial z'} \right] dz'$$
$$= -\left[\frac{\partial (h_a \overline{T}^s_{x'x'})}{\partial x'} + \frac{\partial (h_a \overline{T}^s_{y'x'})}{\partial y'} \right] + T^s_{z'x'b} \tag{11}$$

Following Savage and Hutter (1989), we can relate the depth-averaged normal stresses $\overline{T}^s_{x'x'}$ and $\overline{T}^s_{y'y'}$ to the depth-averaged z' direction normal stress $\overline{T}^s_{z'z'}$ by using a lateral stress coefficient $k_{act/pass}$ derived from Coulomb theory

$$\overline{T}^s_{x'x'} = \overline{T}^s_{y'y'} = k_{act/pass} \overline{T}^s_{z'z'} \tag{12}$$

where $k_{act/pass}$ is also called the Earth pressure coefficient. If the internal behavior of the granular material is frictional, $k_{act/pass}$ can be given by (Iverson, 1997; Savage and Hutter, 1989)

$$k_{act/pass} = 2 \frac{1 \mp [1 - \cos^2 \phi_{int}(1 + \tan^2 \phi_{bed})]^{1/2}}{\cos^2 \phi_{int}} - 1 \tag{13}$$

where ϕ_{int} is the internal friction angle of the granular solid and ϕ_{bed} is the friction angle of grains contacting the bed. The sign $\mp$ is negative (and $k_{act/pass}$ active) for diverging flow (indicated by $\frac{\partial u_a}{\partial x'} + \frac{\partial v_a}{\partial y'} > 0$) and positive (and $k_{act/pass}$ passive) for converging flow (indicated by $\frac{\partial u_a}{\partial x'} + \frac{\partial v_a}{\partial y'} < 0$). This expression is valid if $\phi_{bed} < \phi_{int}$. If, on the other hand, $\phi_{bed} > \phi_{int}$, $k_{act/pass}$ is given by

$$k_{act/pass} = \frac{1 + \sin^2 \phi_{int}}{1 - \sin^2 \phi_{int}} \tag{14}$$

The transverse solid shear stresses $\overline{T}^s_{y'x'}$ and $\overline{T}^s_{x'y'}$ are related to the normal stresses and can be written as

$$\overline{T}^s_{y'x'} = \overline{T}^s_{x'y'} = -sgn(S_{x'y'}) \left[\frac{1}{2} k_{act/pass}(1 - \lambda) \rho g_{z'} h_a \right] \sin \phi_{int} \tag{15}$$

where $S_{x'y'}$ is the rate of strain in the $x' - y'$ plane. The basal shear stress $T^s_{z'x'b}$ is obtained by using the well-known Coulomb-type friction law

$$T^s_{z'x'b} = -T^s_{z'z'b} \tan \phi_{bed} = -[(1 - \lambda) \rho g_{z'} h_a] \tan \phi_{bed} \frac{u_a}{\sqrt{u_a^2 + v_a^2}} \tag{16}$$

with a corresponding expression for $T^s_{z'y'b}$.

2.1.2. Evaluation of fluid stresses

The depth-averaged fluid stresses in the x' direction momentum equation are formulated as

$$-\int_0^{h_a} \left[\frac{\partial T^f_{x'x'}}{\partial x'} + \frac{\partial T^f_{y'x'}}{\partial y'} + \frac{\partial T^f_{z'x'}}{\partial z'} \right] dz'$$
$$= -\int_0^{h_a} \left[\frac{\partial P^f}{\partial x'} - \gamma_f \mu \left(\frac{\partial^2 v_{x'}}{\partial x'^2} + \frac{\partial^2 v_{x'}}{\partial y'^2} + \frac{\partial^2 v_{x'}}{\partial z'^2} \right) \right] dz' \tag{17}$$

where γ_f is the fluid volume fraction in the landslide and μ is Newtonian dynamic viscosity. Using Leibniz' rule, we get

$$-\int_0^{h_a} \frac{\partial P^f}{\partial x'} dz' = -\left[\frac{\partial}{\partial x'} \left(\int_0^{h_a} P^f dz' \right) - \frac{\partial h_a}{\partial x'} P^f_h \right]$$
$$= -\frac{\partial (h_a \overline{P}^f)}{\partial x'} + \frac{\partial h_a}{\partial x'} P^f_h \tag{18}$$

From Eq. (5), we obtain the depth-averaged fluid pressure as

$$\overline{P}^f = P^f_h + \frac{1}{2} \lambda \rho g_{z'} h_a \tag{19}$$

Fig. 1. Sketch of the landslide and the slope-oriented coordinate system. α is the bed slope angle. The slide height in the slope-oriented coordinate system h_a is correlated with the upper layer thickness. A and B are two neighboring grid points in the slope-oriented coordinate. The slide thickness in the (x, z) coordinate h_s can be estimated by $0.5(h_{aA} + h_{aB}))/\cos\alpha$.

Plugging Eq (19) into Eq. (18) gives

$$-\int_0^{h_a} \frac{\partial P^f}{\partial x'} dz' = -h_a \frac{\partial P_h^f}{\partial x'} - \frac{\partial}{\partial x'}\left(\frac{1}{2}\lambda\rho g_{z'} h_a^2\right) \tag{20}$$

We further assume that the fluid shear stresses in Eq. 17 are negligible, considering that they are much smaller than the Coulomb friction. The slope-parallel diffusion terms are also negligible, due to the relatively larger horizontal length scale in the landslide. The depth averaged solid and fluid stresses in the y' direction momentum equation can be obtained following the same procedure as above.

2.1.3. Conservative form of the granular flow equations

The granular flow equations are solved by using a Harten-Lax-vanLeer (HLL) approximate Riemann solver. In order to apply the HLL shock-capturing scheme, we have write the governing equations in a conservative form given by

$$\frac{\partial \mathbf{U}}{\partial t} + \frac{\partial \mathbf{F}}{\partial x'} + \frac{\partial \mathbf{G}}{\partial y'} = \mathbf{S} \tag{21}$$

in which $\mathbf{U} = (h_a, h_a u_a, h_a v_a)^T$. The fluxes are

$$\mathbf{F} = \begin{pmatrix} h_a u_a \\ h_a u_a^2 + \frac{1}{2}[(1-\lambda)k_{act/pass} + \lambda]g_{z'} h_a^2 \\ h_a u_a v_a \end{pmatrix} \tag{22}$$

$$\mathbf{G} = \begin{pmatrix} h_a v_a \\ h_a u_a v_a \\ h_a v_a^2 + \frac{1}{2}[(1-\lambda)k_{act/pass} + \lambda]g_{z'} h_a^2 \end{pmatrix} \tag{23}$$

The source term is

$$\mathbf{S} = \begin{pmatrix} 0 \\ S_{x'} \\ S_{y'} \end{pmatrix} \tag{24}$$

where

$$S_{x'} = g_{x'} h_a - \frac{h_a}{\rho}\frac{\partial P_h^f}{\partial x'} - (1-\lambda)g_{z'} h_a \tan\phi_{bed} \frac{u_a}{\sqrt{u_a^2 + v_a^2}} \tag{25}$$

$$-\,\mathrm{sgn}(S_{x'y'})h_a k_{act/pass}\frac{\partial}{\partial y'}[g_{z'} h_a(1-\lambda)]\sin\phi_{int}$$
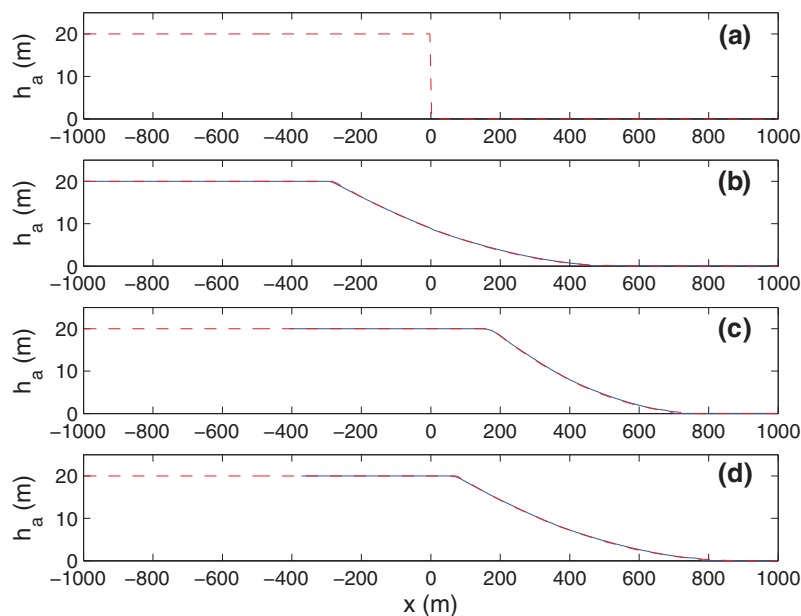

Fig. 2. Verification of the granular flow model using analytical solutions of Mangeney et al. (2000) for a frictional dam break debris flow onto a numerically dry surface. Panel (a): initial profile of the dam-break on the slope; (b): bed slope $\alpha = 0°$ with no friction ($\phi_{bed} = 0°$) at $t = 20$ s; (c): bed slope $\alpha = 20°$ with no friction ($\phi_{bed} = 0°$) at $t = 15$ s; (d): bed slope $\alpha = 20°$ with friction ($\phi_{bed} = 10°$) at $t = 20$ s. The initial height of the dam in all cases is $h_a = h_0 = 20$ m. Solid lines: simulations; dashed lines: analytical solutions.

$$S_{y'} = g_{y'} h_a - \frac{h_a}{\rho} \frac{\partial P_h^f}{\partial y'} - (1-\lambda) g_{z'} h_a \tan \phi_{bed} \frac{v_a}{\sqrt{u_a^2 + v_a^2}} \qquad (26)$$

$$-sgn(S_{y'x'}) h_a k_{act/pass} \frac{\partial}{\partial x} [g_{z'} h_a (1-\lambda)] \sin \phi_{int}$$

where λ is a parameter to be determined.

2.2. Tsunami wave generation

Tsunami wave generation and propagation is simulated using the 3D Non-Hydrostatic WAVE model NHWAVE (Ma et al., 2012). NHWAVE solves the incompressible Navier–Stokes equations in well-balanced conservative form, formulated in time-dependent surface and terrain-following σ coordinates defined by

$$t = t^* \quad x = x^* \quad y = y^* \quad \sigma = \frac{z^* + h}{D}$$

where (x^*, y^*, z^*) is the traditional Cartesian coordinate system with z^* oriented upwards against gravity and the still water surface lying in the (x^*, y^*) plane. Total water depth is given by $D(x, y, t) =$ $h(x, y, t) + \eta(x, y, t)$, where h is the water depth from the still water level to the landslide surface, which is temporally varying during landslide motion, and η is water surface elevation relative to still water. In keeping with the σ coordinate approach, h and η are assumed to remain single-valued functions of (x, y) at all times.

Following Ma et al. (2012), well-balanced mass and momentum conservation equations in σ coordinates are given by

$$\frac{\partial D}{\partial t} + \frac{\partial Du}{\partial x} + \frac{\partial Dv}{\partial y} + \frac{\partial \omega}{\partial \sigma} = 0 \qquad (27)$$

$$\frac{\partial \mathbf{U}}{\partial t} + \frac{\partial \mathbf{F}}{\partial x} + \frac{\partial \mathbf{G}}{\partial y} + \frac{\partial \mathbf{H}}{\partial \sigma} = \mathbf{S}_h + \mathbf{S}_p \qquad (28)$$

where $\mathbf{U} = (Du, Dv, Dw)^T$. (u, v, w) are velocity shows components in (x, y, z) directions. ω is the velocity normal to a level σ surface. The fluxes in the momentum equations are
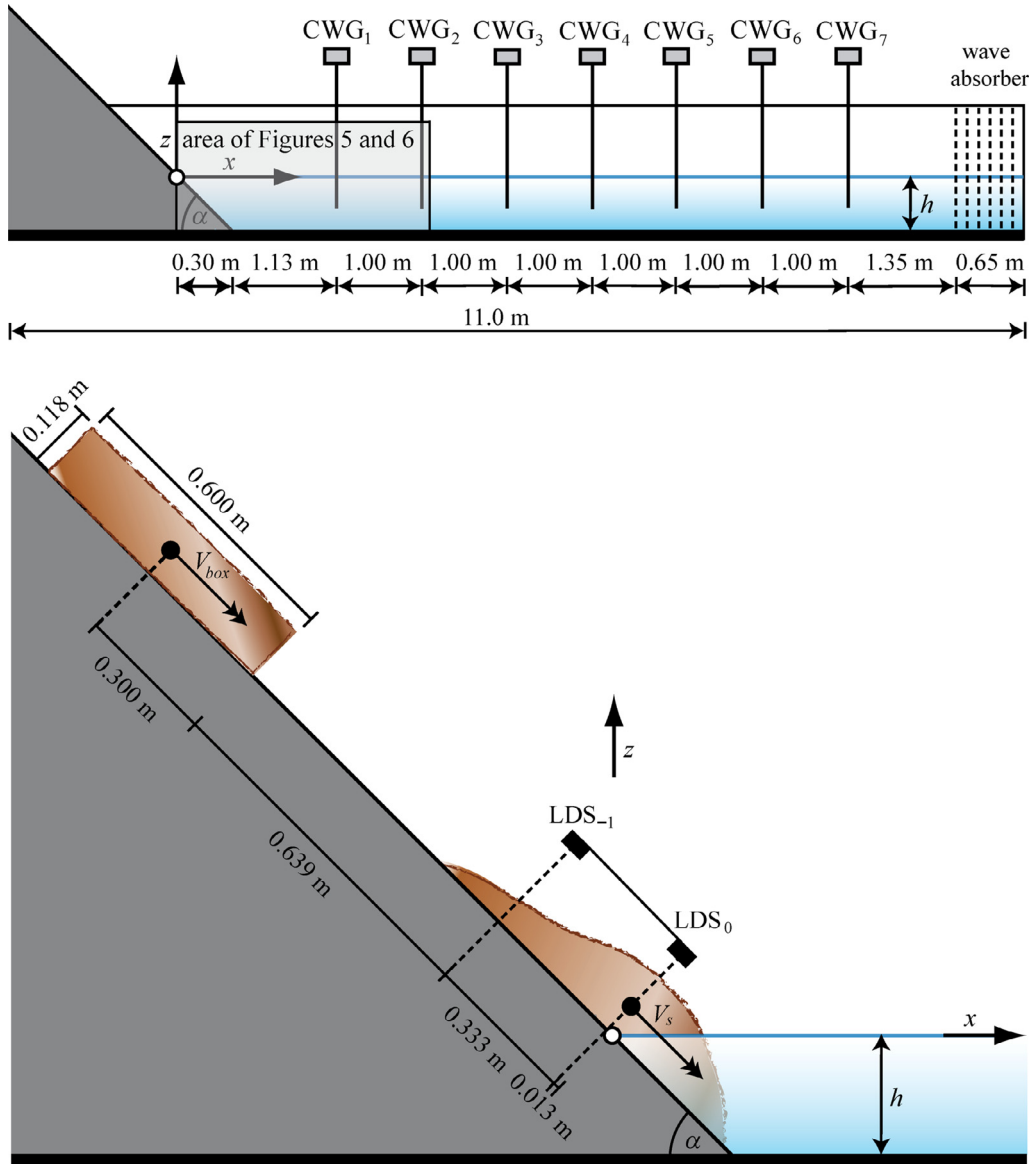

Fig. 3. Upper panel: the setup of wave flume and the positions of seven capacitance wave gages along channel axis. The angle of the slope is $\alpha = 45°$. The still water depth $h = 0.3$ m. Lower panel: the position of the landslide, which is 0.6 m long and 0.118 m high. The evolution of the landslide profile is recorded by two Laser Distance Sensors (LDSs) (from Heller, 2007).

$$\mathbf{F} = \begin{pmatrix} Duu + \frac{1}{2}g\eta^2 + gh\eta \\ Duv \\ Duw \end{pmatrix} \quad \mathbf{G} = \begin{pmatrix} Duv \\ Dvv + \frac{1}{2}g\eta^2 + gh\eta \\ Dvw \end{pmatrix}$$

$$\mathbf{H} = \begin{pmatrix} u\omega \\ v\omega \\ w\omega \end{pmatrix}$$

The source terms on the right hand side of Eq. (28) are contributions from hydrostatic pressure and dynamic pressure, respectively. The turbulent diffusion terms have been ignored. These terms can be formulated as

$$\mathbf{S}_h = \begin{pmatrix} g\eta\frac{\partial h}{\partial x} \\ g\eta\frac{\partial h}{\partial y} \\ 0 \end{pmatrix} \quad \mathbf{S}_p = \begin{pmatrix} -\frac{D}{\rho^f}\left(\frac{\partial p}{\partial x} + \frac{\partial p}{\partial \sigma}\frac{\partial \sigma}{\partial x*}\right) \\ -\frac{D}{\rho^f}\left(\frac{\partial p}{\partial y} + \frac{\partial p}{\partial \sigma}\frac{\partial \sigma}{\partial y*}\right) \\ -\frac{1}{\rho^f}\frac{\partial p}{\partial \sigma} \end{pmatrix}$$

where p is the non-hydrostatic component of the pressure field. Further details of the model may be found in Ma et al. (2012).

2.3. Interaction between landslide and water

The governing equations describing the lower-layer landslide and upper-layer water motion are derived in two different coordinate systems. The granular landslide model is built in a slope-oriented coordinate system with z' perpendicular to the bottom, while the upper-layer water motion is described in a regular Cartesian coordinate system with z vertical. To calculate the upper-layer thickness, it is necessary to find the landslide height in the vertical z direction, indicated by h_s in Fig. 1. With the given bottom slope α, h_s can be estimated as $0.5(h_{aA} + h_{aB})/\cos\alpha$, where h_{aA} and h_{aB} are the predicted landslide heights in the z' direction at two neighboring grid points as demonstrated in Fig. 1. In addition, the streamwise gradients in two coordinate systems are related as $\partial/\partial x' = \cos\alpha\,\partial/\partial x$. The orientation of bed slope in y direction can be treated in the same manner.

Interaction between the landslide and water are accounted for by imposing continuity of normal stress (pressure P_h^f) at the interface,

and by using the kinematic interfacial constraints for each layer. The shear stresses at the landslide-water interface are negligible for laboratory scale granular landslides. More studies on their effects on huge landslide motion have to be further studied. Mixing at the landslide-water interface has also been ignored. In test simulations, we find that the pressure P_h^f, which includes both the hydrostatic and non-hydrostatic components, dominates the interactions between two-layer flows, and that contributions from lateral interfacial stresses are negligible. The pressure at the interface is given by

$$P_h^f = \rho^f g(h + \eta) + p(-h) \tag{29}$$

where $p(-h)$ represents the nonhydrostatic component of fluid pressure at the slide surface.

The boundary conditions at the landslide-water interface for the upper-layer equations have to take into account the temporal variation of water depth. Hence, the boundary condition for the vertical velocity is given by

$$w|_{z=-h} = -\frac{\partial h}{\partial t} - u\frac{\partial h}{\partial x} - v\frac{\partial h}{\partial y} \tag{30}$$

where the horizontal gradients of water depth h are also temporally varying and have to be updated at each time step. The boundary condition for dynamic pressure is derived from the momentum equation for w (Ma et al., 2012). The linearized boundary condition for dynamic pressure is written as

$$\frac{\partial p}{\partial \sigma}|_{\sigma=0} = \rho(h + \eta)\frac{\partial^2 h}{\partial t^2} \tag{31}$$

2.4. Numerical scheme

The equations for the lower-layer landslide (Eq. (23)) and upper-layer water motion (Eqs. (30) and (31)) are solved using the same numerical framework for spatial differencing and time-stepping. For the upper-layer water motion, the details of the numerical scheme can be found in Ma et al. (2012) and are not repeated here. For the lower-layer granular landslide, the governing Eq. (23) is also discretized by a second-order finite volume method. The HLL approximate Riemann solver is used to estimate the fluxes at cell faces. In order to apply the Riemann method, we need to compute the speeds and directions of elementary waves that determine fluxes of the conserved variables $\mathbf{U}$
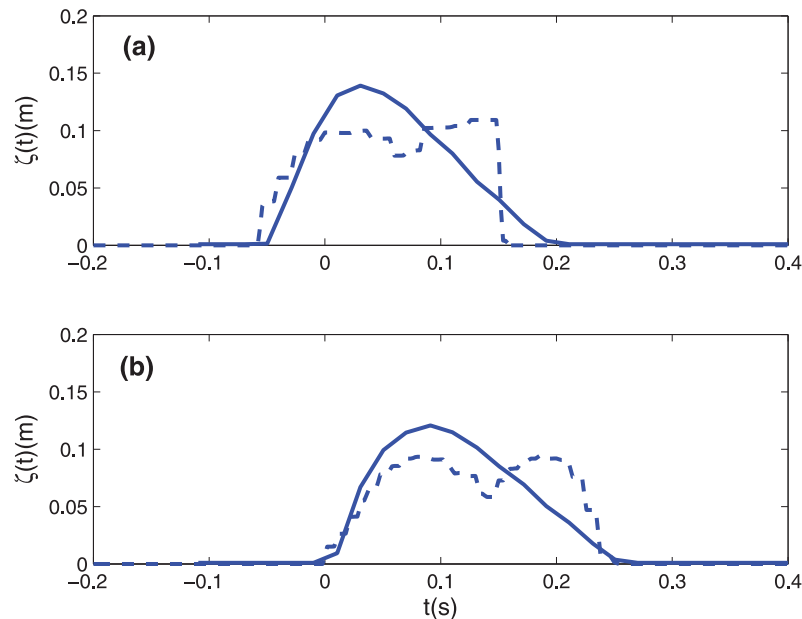

Fig. 4. The comparisons of simulated (solid lines) and measured (dashed lines) landslide profiles recorded at (a) LDS$_{-1}$ and (b) LDS$_0$.
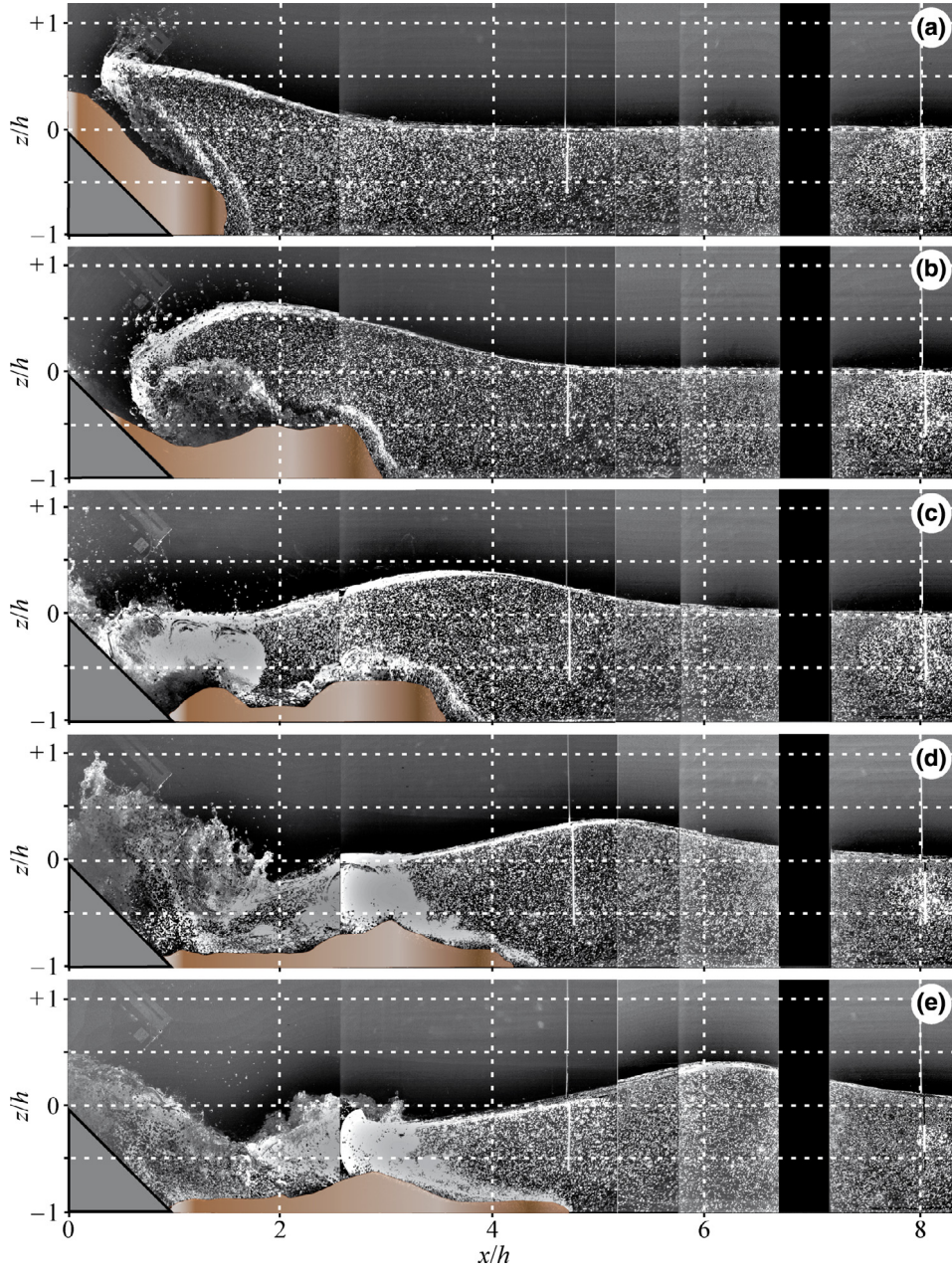
Fig. 5. PIV raw images recorded at $t_r = t(g/h)^{1/2} =$ (a) 1.14; (b) 2.29; (c) 3.43; (d) 4.57 and (e) 5.72 after slide impact (from Heller, 2007).

by propagating information about **U** in space and time (Toro, 1997). To characterize these mathematical waves, we rewrite Eq. (23) using the chain rule as (Denlinger and Iverson, 2001)

$$\frac{\partial \mathbf{U}}{\partial t} + \mathbf{A} \cdot \frac{\partial \mathbf{U}}{\partial x'} + \mathbf{B} \cdot \frac{\partial \mathbf{U}}{\partial y'} = \mathbf{S} \tag{32}$$

where

$$\mathbf{A} = \frac{\partial \mathbf{F}}{\partial \mathbf{U}} = \begin{bmatrix} 0 & 1 & 0 \\ c^2 - u_a^2 & 2u_a & 0 \\ -u_a v_a & v_a & u_a \end{bmatrix} \tag{33}$$

and

$$\mathbf{B} = \frac{\partial \mathbf{G}}{\partial \mathbf{U}} = \begin{bmatrix} 0 & 0 & 1 \\ -u_a v_a & v_a & u_a \\ c^2 - v_a^2 & 0 & 2v_a \end{bmatrix} \tag{34}$$

and c is the speed of ideal gravity waves given by

$$c = \sqrt{[(1-\lambda)k_{act/pass} + \lambda]g_z h_a} \tag{35}$$

The gravity wave speed c in the granular flow equations is fundamentally different from that in the standard shallow-water equations. It considers the effects of Coulomb friction and denotes the maximum rate of information propagation due to lateral stress transfer in the grain-fluid mixture. With the calculated gravity wave speed c, the flux at the cell interface is determined by

$$\mathbf{F}(\mathbf{U}^L, \mathbf{U}^R) = \begin{cases} \mathbf{F}(\mathbf{U}^L) & \text{if } s_L \geq 0 \\ \mathbf{F}^*(\mathbf{U}^L, \mathbf{U}^R) & \text{if } s_L < 0 < s_R \\ \mathbf{F}(\mathbf{U}^R) & \text{if } s_R \leq 0 \end{cases} \tag{36}$$

where

$$\mathbf{F}^*(\mathbf{U}^L, \mathbf{U}^R) = \frac{s_R \mathbf{F}(\mathbf{U}^L) - s_L \mathbf{F}(\mathbf{U}^R) + s_L s_R (\mathbf{U}^R - \mathbf{U}^L)}{s_R - s_L} \tag{37}$$

with wave speed s_L and s_R defined by

$$s_L = \min(u_L - c_L, u_s - c_s) \tag{38}$$

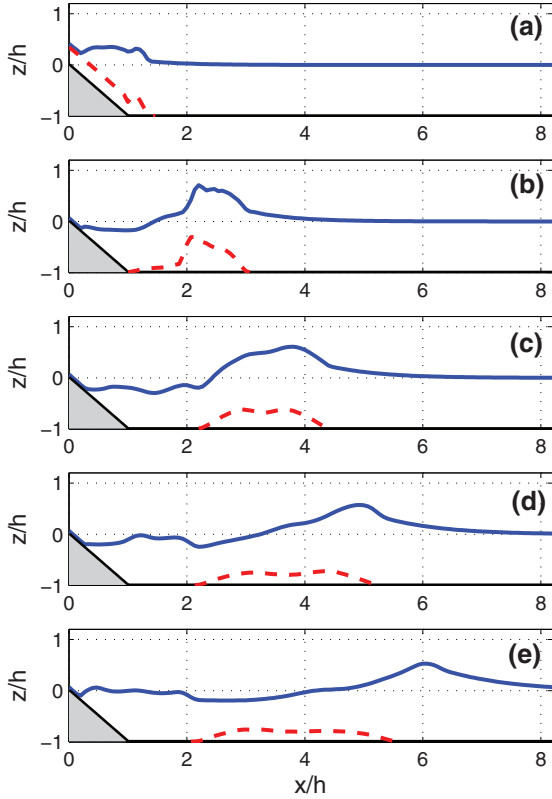$$s_R = \max(u_R + c_R, u_s + c_s) \tag{39}$$

Fig. 6. The simulated impulse wave generation and granular landslide motion at $t_r = t(g/h)^{1/2} =$ (a) 2.29; (b) 3.43; (c) 4.57; (d) 5.72 and (e) 6.86 after slide impact. The solid lines show the free surface elevations, while the dashed lines display the interfaces between the granular landslide and water.

Table 1
Two-dimensional granular landslide parameters (Heller and Hager, 2010).

Description	Symbol	Value
Still water depth	h	0.3 m
Slide length	l_s	0.6 m
Slide thickness	s	0.118 m
Slide impact thickness	s_i	0.095 m
Slide initial velocity	v_s	3.25 m/s
Slide centroid impact velocity	v_{si}	4.67 m/s
Bulk slide density	ρ_s	1,678 kg/m^3
Grain density	ρ_g	2,745 kg/m^3
Grain diameter	d_g	4 mm
Bulk slide porosity	n	0.389
Hill slope angle	α	45°
Dynamic bed friction angle	ϕ_{bed}	24°
Internal friction angle	ϕ_{int}	34°
Slide Froude number	F	2.72
Relative slide thickness	S	0.32
Relative slide mass	M	1.25

dam break debris on a plane bed. The landslide material has no bed friction. The second and third scenarios are the dam breaks on a slope bed with the slope angle of 20°. The bed friction angles of the granular material are 0° and 20°, respectively. As we can see, the simulations match very well with the analytical solutions for all three scenarios. The mean relative errors for these three simulations in the dam-break front regions are 1.53, 3.20 and 2.39%, respectively, where the relative error is defined as $|x_c - x_a|/x_a \times 100\%$ with x_c being the computed value and x_a being the analytical solution. These results indicate that the model can well capture the granular flow motion.

4. Impulsive wave generation by a granular landslide in a two-dimensional wave flume

Impulsive wave generation by granular landslides have been extensively studied in laboratory experiments (for example, Fritz et al., 2004; Heller and Hager, 2010; Mohammed and Fritz, 2012). In this section, we employ the laboratory measurements of Heller and Hager (2010) to validate our two-layer granular landslide model. The experiments were conducted in a prismatic water wave channel of 11 m length, 0.5 m width and 1.0 m depth. The granular landslide material was contained in a slide box which was accelerated by a pneumatic landslide generator down a 3-m-long hill slope ramp. As the slide box reached the maximum velocity, its front flap opened. The landslide left the box, accelerated further down the hill slope ramp due to gravitational forcing, and entered the water column, generating impulse waves in the wave channel (Heller and Hager, 2010). In the selected test case, the slide box has a size of 0.6 m length and 0.118 m height as demonstrated in Fig. 3. The granular landslide material has a grain diameter $d_g = 4$ mm, an internal friction angle $\phi_{int} = 34°$, a grain density $\rho_g = 2,745$ kg/m^3, and a bulk slide density $\rho_s = \rho_g(1 - n) = 1,678$ kg/m^3 with a bulk slide porosity $n = 0.389$. The dynamic bed friction angle is $\phi_{bed} = 24°$. The landslide had an initial velocity of 3.25 m/s when it was released. The properties of the landslide are listed in Table 1. The still water depth is 0.3 m. The landslide profiles were recorded by two laser distance sensors (LDS). Their locations are shown in Fig. 3. The impulse waves were measured at seven wave gauges which are also displayed in Fig. 3.

2D simulations are conducted using only one grid cell in the transverse direction of the wave channel. The length of the computational domain is the same as that of the channel in the experiment, which is 11 m. The horizontal extent of the domain is discretized by 550 grid cells with grid size of 0.02 m. Three vertical levels are used to simulate the upper-layer water motion. For the granular landslide, we choose the same landslide material parameters as those in the experiment. The Earth pressure coefficient $k_{act/pass}$ is calculated by Eq. (13). For
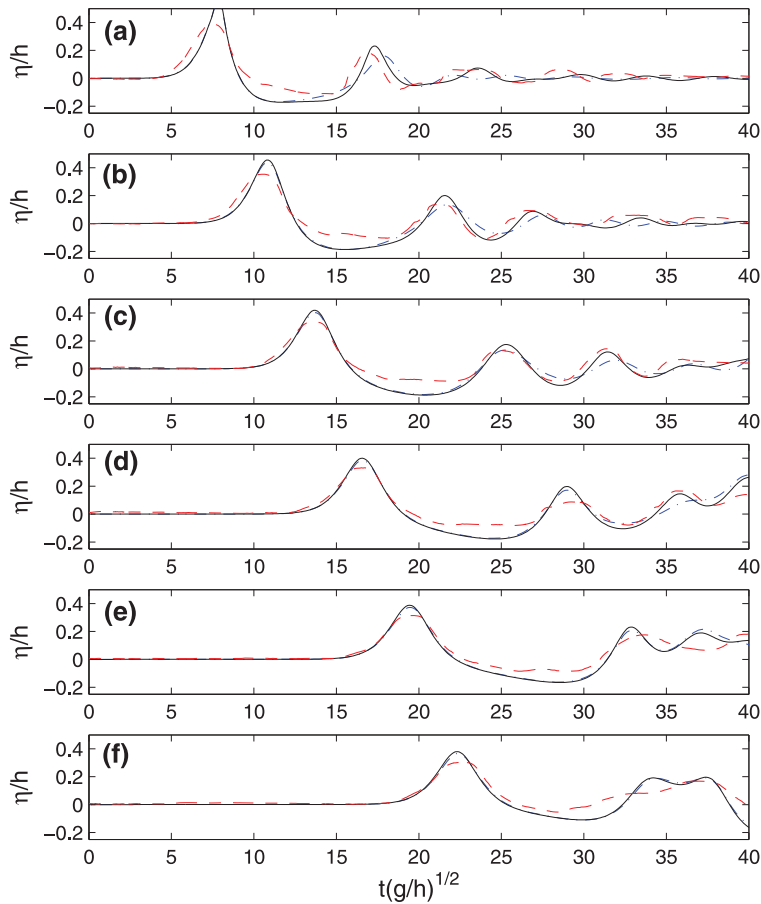
where u_s and c_s are estimated by

$$u_s = \frac{1}{2}(u_L + u_R) + c_L - c_R \qquad (40)$$

$$c_s = \frac{c_L + c_R}{2} + \frac{u_L - u_R}{4} \qquad (41)$$

where $\mathbf{U}^L$ and $\mathbf{U}^R$ are the left and right values of $\mathbf{U}$ at the cell face.

3. Verification of the granular flow model using an analytical solution

We first verify the granular flow model using the analytical solution of Mangeney et al. (2000) for a frictional dam break debris flow onto a numerical dry surface. The analytical solution for the fluid height is given by

$$h_a = \frac{1}{9g\cos\alpha}\left(\frac{x}{t} - 2c_0 + \frac{1}{2}mt\right)^2 \qquad (42)$$

where g is gravitational acceleration, α is the angle of the bed slope, t is time, x is the coordinate with $x = 0$ located at the front of the dam at $t = 0$ s, $c_0 = \sqrt{gh_0\cos\alpha}$ and $m = -g\sin\alpha + g\cos\alpha\tan\phi_{bed}$. This formula is valid in the region defined by $x_L < x < x_R$, where $x_L = -c_0 t - \frac{1}{2}mt^2$ and $x_R = 2c_0 t - \frac{1}{2}mt^2$.

To be consistent with the analytical solution, we set the pressure at the landslide-water interface $P_h^f = 0$ Pa. The parameter λ is set to be 0, consistent with the assumption of a dry granular flow. The Earth pressure coefficient $k_{act/pass}$ is 1.0. The fluid stress given in Eq. (22) is also neglected. The computational domain is 2 km long, with $x < 1$ km occupied by the granular material. The initial height of the dam is $h_0 = 20$ m. Fig. 2 the comparisons of numerical results and analytical solutions for three scenarios. The first scenario represents the

Fig. 7. The comparisons of simulated (solid and dash-dotted lines) and measured (dashed lines) impulse waves at 6 wave gauges (gauge 2–7) generated by a 2D laboratory granular landslide (Heller and Hager, 2010). The solid lines show the simulation results with $\lambda = 0.5$; the dash-dotted lines show the simulation results with $\lambda = 0.2$.

portions of slides located above the water line and exposed to the atmosphere, the fluid pressure at the interface $P_h^f = 0$. We assume that the granular material is dry before water entry, and thus the parameter λ is set to be zero in the subaerial environment.

To accurately predict the tsunami wave generation by granular landslides, it is very important to capture the granular landslide motion and evolution of its profile. Therefore, we first compare the simulated granular landslide profiles with the measurements, as shown in Fig. 4. Time $t = 0$ s is taken to be when the front of the landslide reaches the water surface. Because these two LDSs were installed above the water, the landslide profiles were not affected by the landslide-water interactions. As we can see, the present granular flow model can generally predict the landslide motion and its profile evolution. The speed of the landslide front can be estimated from the time lag between these two profiles. The model accurately captures the landslide front location, indicating that the speed of the landslide front is also well predicted by the model. The measured profiles have steep tails because of large internal friction of the landslide material. In the simulation, however, the tails are smoothed out. In addition, the height of the landslide is slightly overpredicted by the model. This overprediction of the landslide height is reduced when the landslide moves closer to the water surface.

Accurate simulation of underwater landslide motion is more difficult due to the intense interactions between the landslide and water. Figs. 5 and 6 show the measured and simulated impulse wave generation, underwater landslide motion and granular deposit. During the landslide impact, the landslide-water interactions are especially complicated with the entrainment of large air cavities. In our two-layer model, we assume that the lower-layer landslide and

upper-layer water remain in contact, and thus the model cannot represent this aspect of the event. In addition, the current model does not account for the modification of Coulomb friction due to changes in bed slope. Because of these two reasons, the landslide at the transition of the bed slope (panel (a) and (b)) is not well simulated. The model slightly overpredicts the height of the slide front in the slope as seen in Fig. 4, which results in the overestimation of impulsively-generated wave heights. As the landslide moves onto the horizontal bed, the gravitational driving force vanishes. The basal sliding friction decreases the landslide velocity until the landslide comes to rest. After comparing the centroid locations of the simulated landslide, it was found that the landslide has almost come to rest at $t_r = 6.86$, where $t_r = t(g/h)^{1/2}$ is the normalized time after landslide impact. From Figs. 5 and 6, we see that the model reasonably simulates the landslide motion, although the predicted centroid locations of the landslide are further offshore compared to the measurements. It is likely caused by the neglect of Coulomb friction increase at the transition of the slope.

Comparisons of simulated and measured waves are given in Fig. 7. Past studies (Fritz et al., 2004) have shown that the characteristics of landslide generated waves were related to the following two dimensionless parameters: the landslide Froude number $F = v_{si}/\sqrt{gh}$ and the dimensionless landslide thickness $S = s_i/h$, where v_{si} and s_i are the centroid impact velocity and landslide thickness at impact, respectively, and h is the still water depth. In the experiment considered here, these two non-dimensional parameters are $F = 2.72$ and $S = 0.32$, respectively. Based on the criteria suggested by Fritz et al. (2004), the impulsively-generated waves fall into the weakly nonlinear oscillatory wave regime $((4 - 7.5S) < F < (6.6 - 8S))$. In the
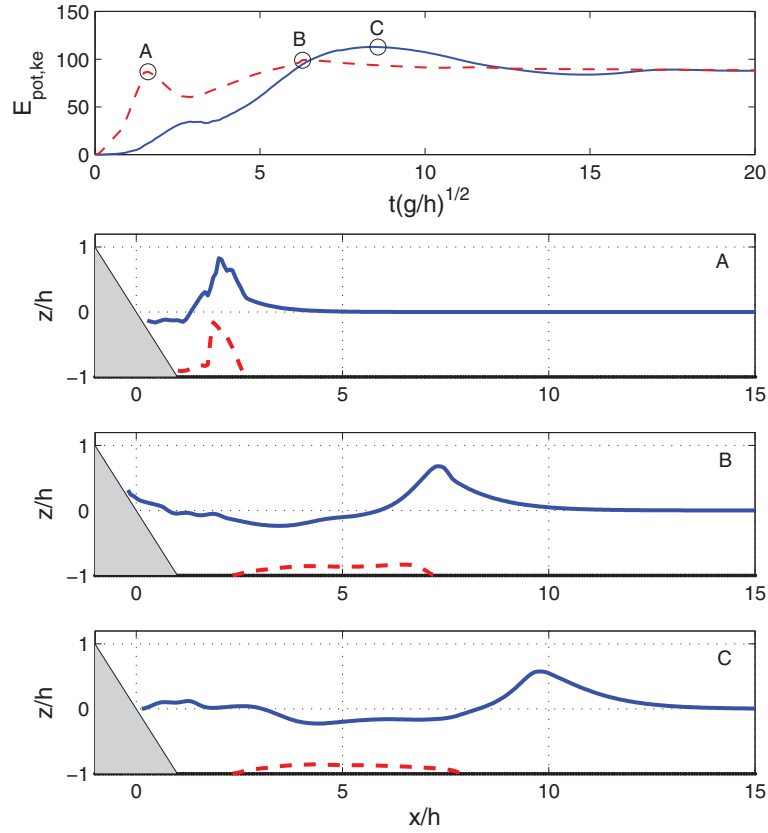
Fig. 8. The upper panel shows the calculated potential energy (solid line) and kinetic energy (dashed line) per unit width for the simulation with $\lambda = 0.5$ after the impact ($t\sqrt{g/h} = 0$ at impact). The potential energy is calculated as $E_{pot} = \frac{1}{2}\rho g \int (\eta - h_a)^2 dx$. The kinetic energy is $E_{ke} = \frac{1}{2}\rho D \int (u^2 + w^2)dxd\sigma$. The lower three panels show the impulse waves (solid lines) as well as the granular landslide (dashed lines) at time A, B and C, corresponding to the peaks of kinetic energy and potential energy indicated in the upper panel.

simulation, the computed landslide centroid impact velocity is 4.10 m/s, which is slightly smaller than the measured value (4.67 m/s). The computed landslide impact thickness is 0.10 m, which is slightly larger than the measured value (0.095 m). The non-dimensional parameters from the simulation are $F = 2.39$ and $S = 0.33$, respectively, indicating that the predicted waves are still weakly nonlinear oscillatory waves. This is confirmed in Fig. 7, from which we see that the waves generated by the granular landslide are reasonably well captured by the model, although the model overpredicts the leading wave heights, especially at the gauges in the near field. The relative errors at gauges 2 and 3 are 42.7 and 23.7%, respectively. In the far field, the leading wave heights are more accurately predicted. For example, the relative errors at gauges 5 and 6 are 16.3 and 18.7%, respectively.

In Fig. 7, we also show the sensitivity of numerical results to the parameter λ. In Eq. (5), we see that the parameter λ determines the pore pressure at the bed. If $\lambda = 0$, the pressure at the bed P_b^f equals that at the landslide–water interface P_h^f, indicating that the fluid pressure inside the granular landslide is constant. This would generate the maximum Coulomb friction for underwater landslide. If $\lambda = 1.0$, the landslide is completely suspended in the water column, and the Coulomb friction at the bed vanishes. Therefore, the parameter λ determines the magnitude of Coulomb friction imposed on the landslide. In Fig. 7, the solid lines show the results with $\lambda = 0.5$, while the dash-dotted lines show the simulation results with $\lambda = 0.2$. We see that the predicted impulse waves are generally similar. The leading wave height is slightly larger with a larger value of λ, which results in a relatively smaller Coulomb friction. The effect of λ is more significant to the second wave. In the current simulations, we assume that

the granular material is completely dry in the subaerial environment. Thus λ is set to be zero before the landslide enters the water column. Therefore, the λ effect on the leading wave is not significant. After the landslide enters the water column, the Coulomb friction is reduced. A larger value of λ will result in a smaller Coulomb friction, resulting in a larger second wave as seen in Fig. 7. The effects of λ on the impulse waves are mostly in the near field. In the far field (panel (f)), the difference of the simulated impulse waves with different values of λ is insignificant.

The interactions between the landslide and surrounding water involve energy conversion. The increase in potential energy in the water layer induced by the landslide can be calculated by

$$E_{pt} = \int_{-(h-h_a)}^{\eta} \rho gz dz - \int_{-h}^{0} \rho gz dz \qquad (43)$$

where h is the initial water depth without landslide, h_a is the landslide thickness, E_{pt} is the total potential energy increase after the landslide impact. The first term on the right hand side evaluates the potential energy after landslide impact, while the second term calculates the potential energy before landslide. The total potential energy increase is contributed by two parts. The first part is due to the static increase of water level with the presence of underwater landslide, which can be estimated as $E_{ps} = \rho g(\eta + h - h_a)h_a$. The second part is due to the generation of impulse waves by the landslide motion, which can be calculated by

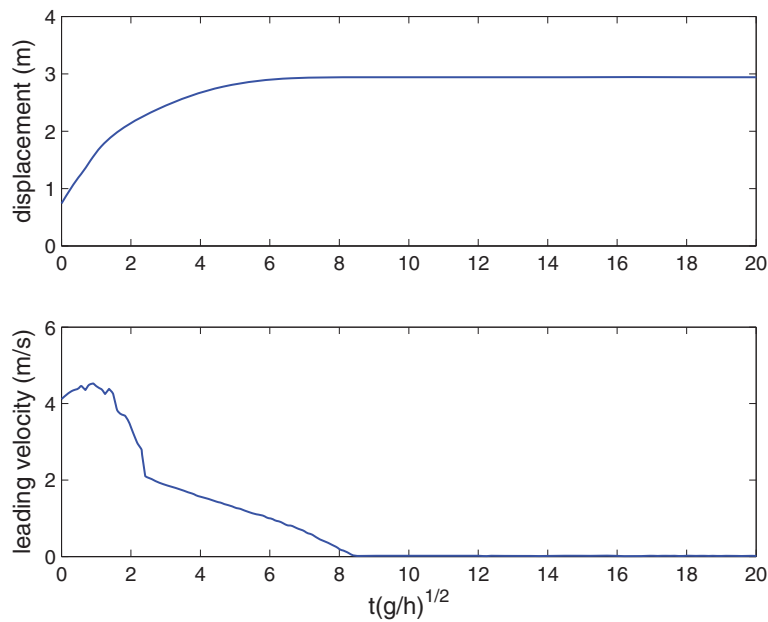$$E_{pw} = E_{pt} - E_{ps} = \frac{1}{2}\rho g(\eta - h_a)^2 \qquad (44)$$

Fig. 9. The predicted landslide displacement and the velocity at the leading edge after slide impact. The break in the curve at $t_r = 2.3$ corresponds to the time when the landslide reaches the horizontal bed.

Thus, the potential energy due to the presence of impulse waves for the whole computational domain can be evaluated as $E_{pot} = \int E_{pw}dx$. The kinetic energy of the impulse waves is $E_{ke} = \frac{1}{2}\rho D \int (u^2 + w^2)dxd\sigma$, where D is the total water depth. Fig. 8 shows the calculated potential energy and kinetic energy of the impulse waves after the landslide impact for the simulation with $\lambda = 0.5$. After the impact, the energy of the landslide is converted to the water column, resulting in the increase of both kinetic energy and potential energy. At the early stage, the kinetic energy increases faster due to the high speed of the landslide. It reaches a peak (peak A) when the landslide hits

the plane bed. The kinetic energy has the maximum value (peak B) when the leading wave crest propagates away from the landslide. The potential energy increases more slowly at the early stage of the subaqueous landslide with the continuous generation of impulse waves, possibly due to the fact that the model is not able to capture the separation of the water and the slide. It reaches the maximum value (peak C) slightly later than that of kinetic energy when the whole leading wave front passes the landslide. At this time, the landslide has almost stopped moving. The interactions between the landslide and surrounding water become weaker. When all the waves pass
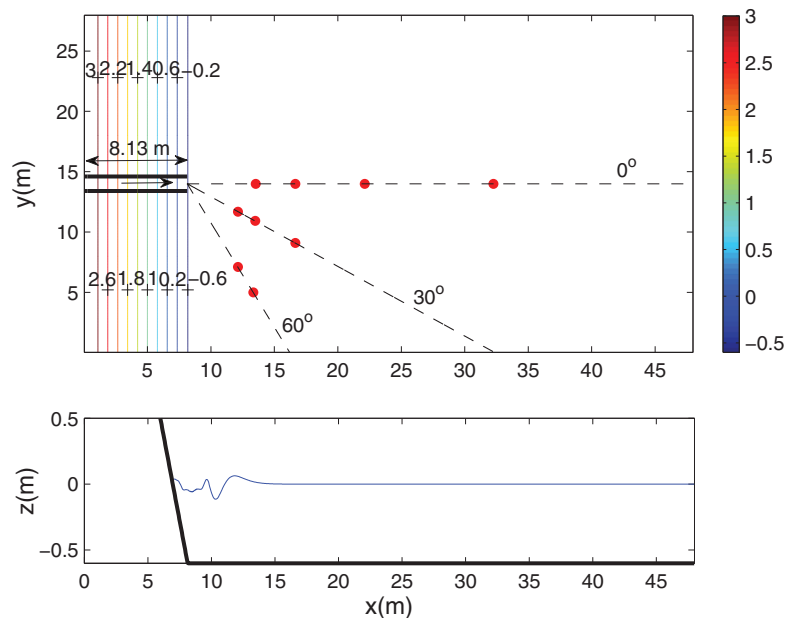

Fig. 10. The computational domain and model setup for Mohammed and Fritz (2012). Upper panel: plan view of the domain. The red dots show the wave gauge array used to measure the water surface elevation. The granular slide collapses down the hillslope with the slope angle of 27.1°. The width of the hillslope is 8.13 m. The contours show the water depth. Lower panel: a transection at $y = 14.0$ m. The free surface is exaggerated for a better view. The still water depth is 0.6 m. (For interpretation of the references to color in this figure legend, the reader is referred to the web version of this article.)

Table 2
Three-dimensional granular landslide parameters (Mohammed and Fritz, 2012).

Description	Symbol	Value
Still water depth	h	0.6 m
Slide length	l_s	1.05 m
Slide width	w_s	1.2 m
Slide thickness	s	0.3 m
Slide impact thickness	s_i	0.072 m
Slide frontal impact velocity	v_{si}	5.72 m/s
Bulk slide density	ρ_s	1,760 kg/m^3
Grain density	ρ_g	2,600 kg/m^3
Grain diameter	d_{50}	13.7 mm
Bulk slide porosity	n	0.31
Hill slope angle	α	27.1°
Dynamic bed friction angle	ϕ_{bed}	23°
Internal friction angle	ϕ_{int}	41°
Slide Froude number	F	1.87
Relative slide thickness	S	0.12
Relative slide mass	M	1.56

by the landslide ($t(g/h)^{1/2} > 16.8$), the potential energy and kinetic energy of the impulse waves are equal, which would be expected from linear theory.

The displacement of the landslide centroid and the velocity at the leading edge after landslide impact are shown in Fig. 9. We can see that the landslide finally stops moving at $t(g/h)^{1/2} = 8.45$ after the impact, when the displacement of the landslide centroid has the maximum value of 2.94 m and the velocity at the leading edge is zero. At the impact, the velocity at the leading edge of the landslide is about 4.12 m/s. This velocity keeps increasing until $t(g/h)^{1/2} = 0.92$ when the landslide reaches the transition of the slope. After then, the landslide front velocity decreases rapidly due to the large resistance at the slope transition. At the plane bed, the leading edge velocity almost decreases linearly because of the Coulomb friction.

5. Tsunami waves generated by a three-dimensional granular landslide

The model is next applied to study tsunami waves generated by a 3D granular landslide. The three-dimensional laboratory experiments were conducted by Mohammed (2010) and Mohammed and Fritz (2012) in the tsunami wave basin at Oregon State University. The basin is 48.8 m in length and 26.5 m in width. The case we choose for this study has a still water depth of 0.6 m. The granular landslide was released on a hillslope, which was inclined at 27.1° with a smooth 9.3 m long steel plate as the sliding surface. The landslide had a volume of 0.378 m^3, initially contained and accelerated in a box with size of 1.05 m × 1.2 m × 0.3 m. The landslide was modeled with naturally rounded river gravel with the following parameters: particle size range from 6.35 to 19.05 mm, $d_{50} = 13.7$ mm, $\rho_g = 2,600$ kg/m^3, landslide bulk density $\rho_s = 1,760$ kg/m^3, porosity $n_{por} = 0.31$, effective internal friction angle $\phi_{int} = 41°$, and dynamic bed friction angle $\phi_{bed} = 23°$. These parameters are summarized in Table 2.

The computational domain and model setup are shown in Fig. 10. The domain size is 48 m in length and 28 m in width, discretized by 960 × 560 grid cells. Three vertical levels are employed to simulate the upper-layer water motion. Slightly different from the laboratory setup, the hillslope covers the whole width of the computational domain with $x < 8.13$ m. The landslide is released in the middle of the hillslope at $y = 14.0$ m. The granular parameters are chosen to be the same as those in the experiment. Again, the earth pressure coefficient $k_{act/pass}$ is calculated by Eq. (13). The parameter λ is taken to be 0.0 above the water and 0.5 after the landslide enters the water column. We validate the model by comparing the tsunami waves at 9 wave gauges displayed in Fig. 11 as red dots.

We first compare the simulated landslide velocity and thickness at impact with the measurements. In the experiment, the landslide impact velocity is 5.72 m/s, resulting in a Froude number $F = v_s/\sqrt{gh} = 1.87$. The landslide thickness at impact is $s = 0.072$ m and the relative landslide thickness is $S = s/h = 0.12$. According to the criteria given by Fritz et al. (2004), the generated tsunamis fall into the category of nonlinear oscillatory waves. The model captures the movement of the granular landslide on the hillslope reasonably well with the predicted landslide thickness at impact $s = 0.078$ m, which is close to the measurement ($s = 0.072$ m). The landslide impact velocity is slightly underestimated with a value of 4.54 m/s. Apparently, the predicted tsunamis are still nonlinear oscillatory waves. This is confirmed in Fig. 11, which shows the comparisons of simulated and measured tsunami waves at 9 wave gauges. Generally, the model simulates the tsunami waves well, although the wave heights are overestimated at some stations; for example, the station with $\theta = 30°$ and $r/h = 7.7$, which is the closest to the shoreline. This indicates that the tsunami waves in the generating area are overpredicted. As discussed in Section 4, three reasons may be used to explain this overprediction. (1) In the current model, the lower-layer landslide and upper-layer water remain in contact, thus the formation of air cavity during landslide impact is not captured; (2) the current model does not account for the increase of Coulomb friction due to the change of curvature at the transition of the slope; (3) the model slightly over-
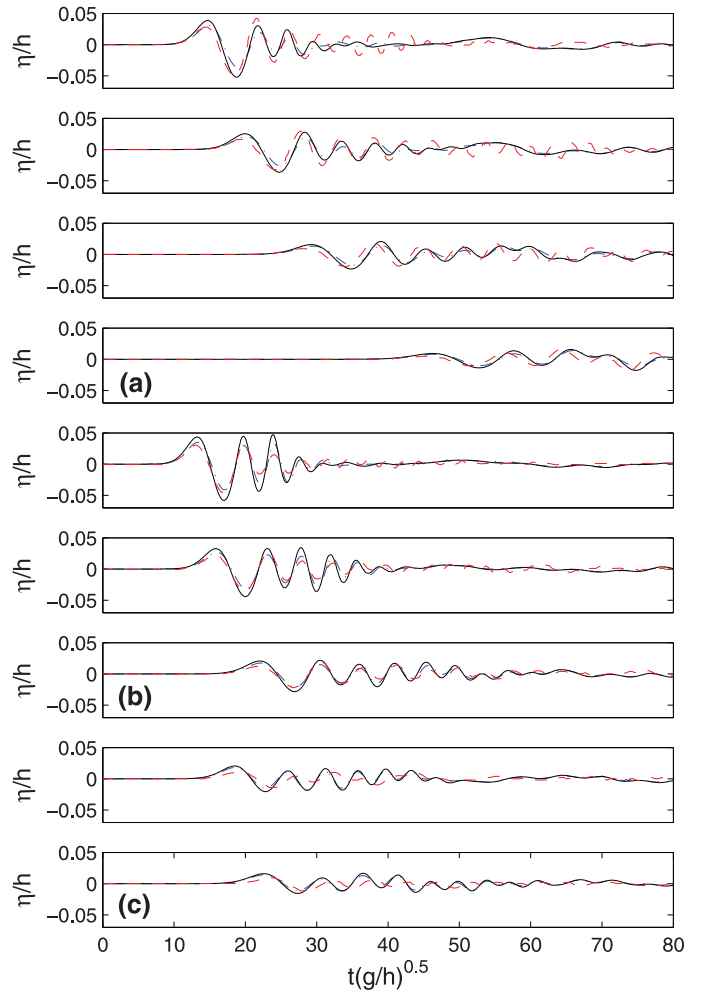

Fig. 11. The comparisons of simulated (solid and dash-dotted lines) and measured (dashed lines) impulse waves at (a) $\theta = 0°$, $r/h = 9.0$, 14.2, 23.3, 40.2; (b) $\theta = 30°$, $r/h = 7.7$, 10.3, 16.4 and (c) $\theta = 60°$, $r/h = 13.3$, 17.3, generated by a 3D laboratory granular landslide (Mohammed and Fritz, 2012). The solid lines show the simulation results with $\lambda = 0.5$; the dash-dotted lines show the simulation results with $\lambda = 0.2$.

predicts the landslide height at the impact. In the far field, the overestimation of wave height decreases and the simulated tsunami waves match well with the measurements. By the end of the time series at stations of $\theta = 0°$ and $r/h = 9.0, 14.2$, the small free surface oscillations are not captured by the model partially due to the relatively coarse horizontal grids used in the simulation.

In Fig. 11, we also demonstrate the results from the simulation with $\lambda = 0.2$. The effects of λ on the impulse waves are similar to the 2D case. The second and third waves are more significantly affected by this parameter compared to the leading wave. The reason has been explained above. Again, this parameter only affects the impulse waves in the generating zone. In the far field, where the waves are not directly generated by the landslide, the results are not sensitive to this parameter.

Figs. 12 and 13 show the simulated landslide motion and tsunami wave generation after the landslide impact. The general patterns of landslide motion and associated tsunami waves are very similar to the laboratory observations (Mohammed and Fritz, 2012). The impact and penetration of the landslide produce an initial wave crest as seen in panel (d). The water displacement develops into a radial wave front with the wave propagating primarily in the direction of the landslide. As the wave front moves away from the shoreline, a wave drawdown is observed on the hillslope in panel (f) followed by a wave run-up. The periodic changes of wave run-up and rundown at the shoreline generate the second wave with radial wave front and the trailing wave train as seen from panel (j) and (l). The 3D landslide motion is more complicated due to the lateral spreading of the granular material compared to the 2D case. After the landslide impact, the landslide width increases dramatically due to the retarding

effect of the water. As the landslide reaches the transition of the slope, the granular material piles up. Over the plane bed, the granular material deposits quickly. The final deposition is found to be located at the plane bed close to the transition of the slope as shown in panel (k), which is more offshore than that observed in the experiments Mohammed (2010) as shown in Fig. 14. The excessive offshore runout of the slide is probably due to the present model's neglect of the additional friction due to the curvature change at the transition of the slope. More accurate simulation of the landslide through the transition of the slope requires a model that is capable of simulating granular flow over 3D irregular terrain.

To examine the effects of non-hydrostatic pressure on tsunami wave generation, we conducted another simulation with the non-hydrostatic pressure correction turned off in NHWAVE. The comparisons of tsunami waves from the non-hydrostatic and hydrostatic simulations are presented in Fig. 15. As expected, wave dispersion is not well captured by the hydrostatic simulation, with wave energy being mostly concentrated in the leading wave. As a result, the granular landslide produces a larger wave in the generating zone with a steeper wave front. Wave height in the hydrostatic simulation decays more rapidly in all directions than that in the non-hydrostatic simulation. These results also confirm that the shallow-water assumption employed by previous researches (i.e. Jiang and Leblond (1992, 1993); Kelfoun et al. (2010) and Giachetti et al., 2011, among others) is probably not valid for tsunami waves generated by rapidly deforming landslides, even for waves being generated in regions with local water depth tending to zero. This was also the conclusion of Ma et al. (2012) for rigid landslides. The non-hydrostatic component of the flow field plays an $O(1)$ role in determining the correct form of
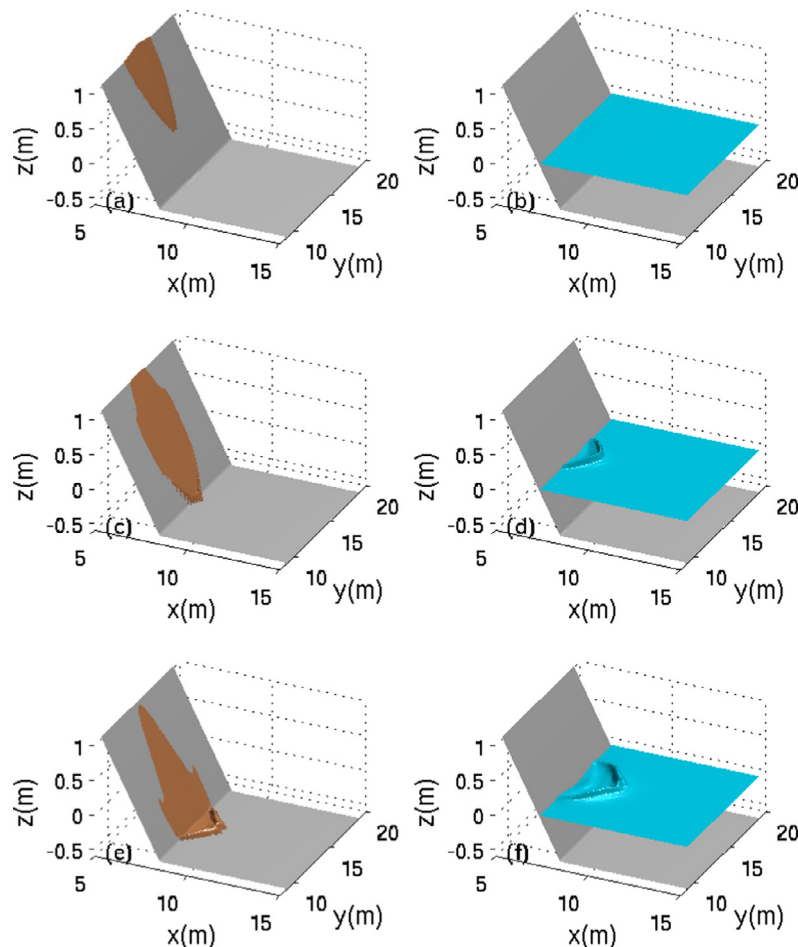

Fig. 12. The simulated granular landslide motion (left panels) and tsunami wave generation (right panels) at t = (a) and (b) 0.0 s; (c) and (d) 0.5 s; (e) and (f) 1.0 s after slide impact.
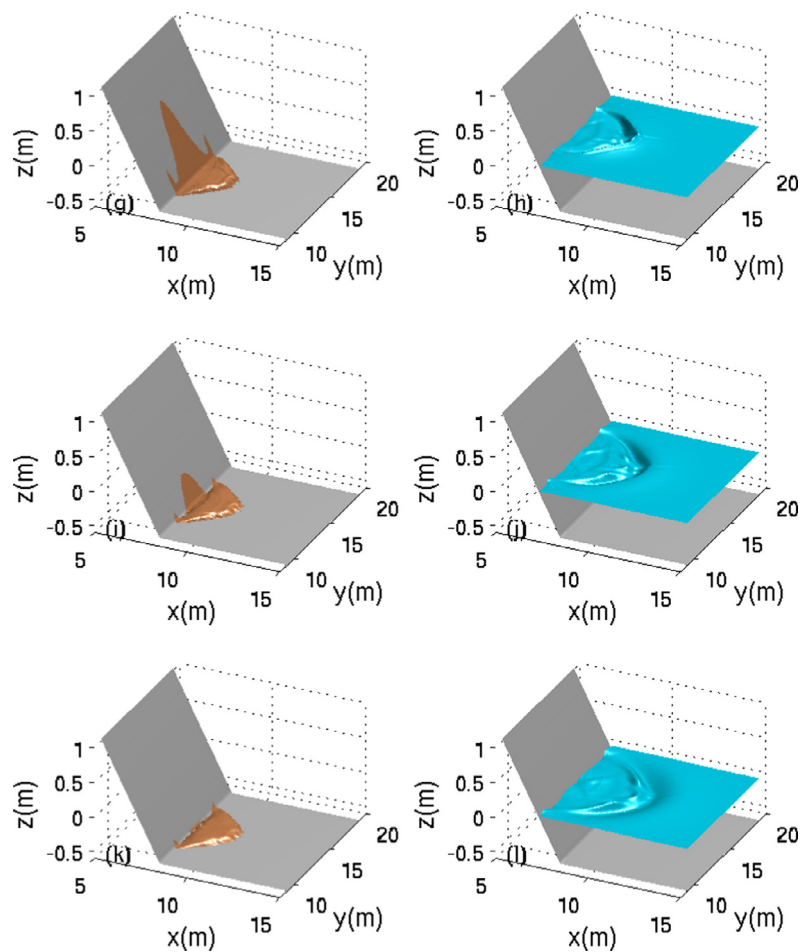
Fig. 13. (Continued) The simulated granular landslide motion (left panels) and tsunami wave generation (right panels) at t = (g) and (h) 1.5 s; (i) and (j) 2.0 s; (k) and (l) 2.5 s after slide impact.
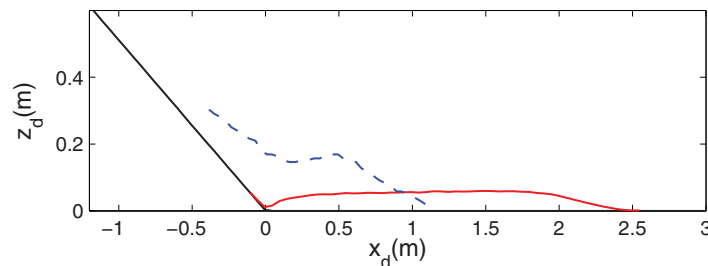

Fig. 14. The comparisons of simulated (red line) and measured (blue dashed line) granular deposits. (For interpretation of the references to color in this figure legend, the reader is referred to the web version of this article.)

the resulting tsunami wave. The sensitivity of model results to computational grids is also presented in Fig. 15, which clearly shows that the simulated impulse waves have negligible differences by increasing the vertical layers. Three vertical levels in NHWAVE are sufficient to capture the impulse wave processes. Fig. 15 also demonstrates the convergence of model results with increasing grid refinement as the simulated impulse waves using coarser grids with $\Delta x = 0.06$ m and $\Delta y = 0.07$ m have negligible differences with those from a fine grid simulation.

6. Conclusions

In this paper, we have developed a model for tsunami generation by deformable granular landslides. The model utilizes a discrete, two-layer formulation to represent the landslide volume and overlying water layer. The landslide is modeled as a depth-integrated granular flow following Savage and Hutter (1989) and Iverson (1997). The landslide model is formulated in slope-oriented coordinates based on the following major assumptions: (1) the characteristic horizontal length scale of the landslide is much greater than the characteristic vertical length scale; (2) the fluid pressure inside the landslide varies linearly with depth; (3) the fluid frictional shear stresses at the landslide-water interface are relatively small compared to the Coulomb friction at the bed; (4) the water surface is a single value function of the horizontal coordinates, the effects of air cavity formation during landslide impact are negligible. The water layer is modeled using the existing non-hydrostatic surface wave model NHWAVE of Ma et al. (2012), with three vertical levels used in the σ coordinate formulation. The two layers are coupled through kinematic boundary conditions and through continuity of normal stresses, and are solved using the same finite-volume approach.
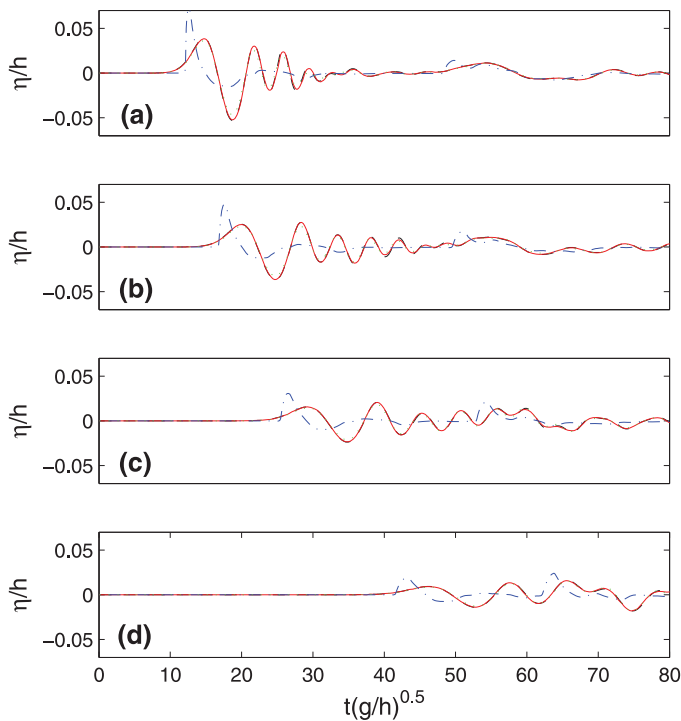
Fig. 15. The comparisons of impulse waves from a non-hydrostatic simulation (solid lines) and a hydrostatic simulation (dash-dotted lines) at $\theta = 0°$, $r/h =$ (a) 9.0, (b) 14.2, (c) 23.3 and (d) 40.2, generated by a 3D granular landslide. The dashed lines show the simulated impulse waves using 5 vertical layers. The dotted lines show the simulated impulse waves using coarser grids ($\Delta x = 0.06$ m, $\Delta y = 0.07$ m).

The two-layer model was validated using analytical solutions for granular dam-break flow as well as measured tsunami waves generated by 2D and 3D laboratory granular landslides. The model simulations illustrate a complex interplay between the granular landslide and associated tsunami waves. Dam-break flow was accurately predicted by the granular flow model employing a shock-capturing numerical scheme. The granular landslide motion as well as tsunami waves generation were all reproduced with reasonable accuracy.

The results here demonstrate the potential usefulness of the granular flow approach in modeling the generation of short, dispersive tsunami waves during landslide events. The present model can be further improved in several respects. First, our model results demonstrate that the predicted tsunami waves are sensitive to the parameter λ (pore pressure at the bed) in the generating zone when the landslide runout distance is long. The determination of this parameter needs to be studied further. Secondly, the Coulomb friction may vary spatially due to changes in local bed slope, which is not completely accounted for in our sample computations. Thirdly, model applications on the submarine granular landslides will have to be validated by experimental data.

Two avenues of further model improvement are being pursued. First, the use of slope-oriented coordinates here facilitates a correct representation of downslope body forces and the resulting vertical acceleration component, but greatly complicates model extension to landslide motion over arbitrary three-dimensional bathymetry. An approach to this problem which retains the use of locally slope-oriented coordinates has been developed by Kelfoun and Druitt (2005) for subaerial landslides, and has subsequently been applied to tsunami generation by Kelfoun et al. (2010) and Giachetti et al. (2011). The formulation requires great care in determining bed curvature effects. Alternately, Denlinger and Iverson (2004) have shown a formulation for the landslide layer in standard Cartesian coordinates with x, y horizontal. In this case, vertical acceleration and its effect on

the pressure field becomes the difficult factor to describe accurately. Denlinger and Iverson (2004) develop a simple explicit estimate for the pressure correction to hydrostatic results using the vertical momentum balance and continuity; the result is analogous to the approach followed by Yamazaki et al. (2009) in their incorporation of non-hydrostatic, dispersive wave effects in a depth-integrated model for the water layer. Alternately, the pressure correction can be evaluated explicitly in terms of higher spatial derivatives of the horizontal motion; this approach leads to equations with forms analogous to Boussinesq equations for the water layer, which are well understood but which greatly complicate the numerical approach to solving the horizontal momentum equations. See, for example, Shi et al. (2012), where the equations for the water layer are solved using the same finite volume TVD scheme as employed here but with extensions to deal with higher-order derivatives. Our preference at this stage in our work is to pursue the approach of Denlinger and Iverson (2004).

The second avenue of future model improvement lies in improving the model for landslide rheology. For the case of saturated or partially saturated granular debris flows, Iverson and George (2014) have recently described a model which maintains the separate identity of solid and fluid phases in the landslide mass, and, in so doing, is able to account for dilatancy effects and rapid changes in rheological properties as landslide motion evolves. The model is capable of maintaining a potential landslide mass in an initial motionless state, with the landslide being initiated by perturbations to the initial configuration. The application of such a model would be a great asset to the process of coupling geotechnical stability analysis with landslide and tsunami hazard assessment. The extension of the present model to incorporate this formulation is relatively straight forward and will be described subsequently.

References

Abadie, S., Harris, J.C., Grilli, S.T., Fabre, R., 2012. Numerical modeling of tsunami waves generated by the flank collapse of the Cumbre Vieja volcano (La Palma, Canary islands): tsunami source and near field effects. J. Geophys. Res. 117, C05030. doi:10.1029/2011JC007646.

Abadie, S., Morichon, D., Grilli, S.T., Glockner, S., 2010. Numerical simulation of waves generated by landslides using a multiple-fluid Navier-Stokes model. Coast. Eng. 57, 779–794.

Assier-Rzadkiewicz, S., Mariotti, C., Heinrich, P., 1997. Numerical simulation of submarine landslides and their hydraulic effects. J. Waterw. Port Coast. Ocean Eng. 123, 149–157.

Ataie-Ashtiani, B., Shobeyri, G., 2008. Numerical simulation of landslide impulsive waves by incompressible smoothed particle hydrodynamics. Int. J. Numer. Meth. Fluids 56, 209–232.

Braathen, A., Blikra, L.H., Berg, S.S., Karlsen, F., 2004. Rock-slope failures in norway: type, geometry, deformation mechanisms and stability. Norw. J. Geol. 84, 67–88.

Denlinger, R.P., Iverson, R.M., 2001. Flow of variably fluidized granular masses across three-dimensional terrain 2. Numerical predictions and experimental tests. J. Geophys. Res. 106 (B1), 553–566.

Denlinger, R.P., Iverson, R.M., 2004. Granular avalanches across irregular three-dimensional terrain: 1. theory and computation. J. Geophys. Res. 109, F01014. doi:10.1029/2003JF000085.

Enet, F., Grilli, S.T., 2007. Experimental study of tsunami generation by three-dimensional rigid underwater landslide. J. Waterw. Port Coast. Ocean Eng. 133, 442–454.

Fine, I., Rabinovich, A., Bornhold, B., Thomson, R., Kulikov, E., 2005. The grand banks landslide-generated tsunami of November 18, 1929: preliminary analysis and numerical modeling. Mar. Geol. 215, 45–57.

Fritz, H.M., Hager, W.H., Minor, H.-E., 2001. Lituya bay case: rockslide impact and wave run-up. Sci. Tsunami Hazards 19, 3–22.

Fritz, H.M., Hager, W.H., Minor, H.-E., 2004. Near field characteristics of landslide generated impulse waves. J. Waterw. Port Coast. Ocean Eng. 130, 287–302.

Fritz, H.M., Hillaire, J.V., Moliere, E., Wei, Y., Mohammed, F., 2012. Twin tsunamis triggered by the 12 January 2010 Haiti earthquake. Pure Appl. Geophys. 170, 1463–1474.

Fritz, H.M., Mohammed, F., Yoo, J., 2009. Lituya bay landslide impact generated megatsunami 50th anniversary. Pure Appl. Geophys. 166, 153–175.

Fuhrman, D.R., Madsen, P.A., 2009. Tsunami generation, propagation, and run-up with a high-order boussinesq model. Coast. Eng. 56, 747–758.

Giachetti, T., Paris, R., Kelfoun, K., Perez-Torrado, F.J., 2011. Numerical modelling of the tsunami triggered by the Guimar debris avalanche, tenerife (Canary islands): comparison with field-based data. Mar. Geol. 284 (1-4), 189–202.

Grilli, S.T., O'Reilly, C., Harris, J.C., Tajali Bakhsh, T., Tehranirad, B., Banihashemi, S., Kirby, J.T., Baxter, C.D.P., Eggeling, T., Ma, G., Shi, F., 2015. Modeling of SMF tsunami hazard along the upper us east coast: detailed impact around ocean city, MD. Nat. Hazards doi:10.1007/s11069-014-1522-8.

Grilli, S.T., Vogelmann, S., Watts, P., 2002. Development of a 3d numerical wave tank for modeling tsunami generation by underwater landslides. Eng. Anal. Bound. Elem. 26 (4), 301–313.

Grilli, S.T., Watts, P., 1999. Modeling of waves generated by a moving submerged body: applications to underwater landslides. Eng. Anal. Bound. Elem. 23, 645–656.

Grilli, S.T., Watts, P., 2005. Tsunami generation by submarine mass failure: 1. Modeling, experimental validation, and sensitivity analysis. J. Waterw. Port Coast. Ocean Eng. 131 (6), 283–297.

Harbitz, C., Pedersen, G., Gjevik, B., 1993. Numerical simulations of large water waves due to landslides. J. Hydraul. Eng. 119, 1325–1342.

Harbitz, C.B., 1992. Model simulations of tsunamis generated by the Storegga slides. Mar. Geol. 105, 1–21.

Harbitz, C.B., Lovholt, F., Bungum, H., 2014. Submarine landslide tsunamis - how extreme and how likely? Nat. Hazards 72, 1341–1374.

Heinrich, P., 1992. Nonlinear water waves generated by submarine and aerial landslides. J. Waterw. Port Coast. Ocean Eng. 118, 249–266.

Heinrich, P., Mangeney, A., Guibourg, S., Roche, R., Boudon, G., Cheminee, J.-L., 1998. Simulation of water waves generated by a potential debris avalanche in Montserrat, Lesser Antilles. Geophys. Res. Lett. 25, 3697–3700.

Heller, V., 2007. Landslide generated impulse waves - prediction of near field characteristics. ETH Zurich Phd dissertation. http://ecollection.ethbib.ethz.ch/view.eth:30012

Heller, V., Hager, W.H., 2010. Impulse product parameter in landslide generated impulse waves. J. Waterw. Port Coastal Ocean Eng. 136, 145–155.

Horrillo, J., Wood, A., Kim, G.-B., Parambath, A., 2013. A simplified 3d Navier–Stokes numerical model for landslide-tsunami: application to the Gulf of Mexico. J. Geophys. Res. Oceans 118, 6934–6950.

Iverson, R.M., 1997. The physics of debris flow. Rev. Geophys. 35, 245–296.

Iverson, R.M., Denlinger, R.P., 2001. Flow of variably fluidized granular masses across three-dimensional terrain 1. Coulomb mixture theory. J. Geophys. Res. 106, 537–552.

Iverson, R.M., George, D.L., 2014. A depth-averaged debris-flow model that includes the effects of evolving dilatancy. 1. Physical basis. Proc. Roy. Soc. A 470, 20130819.

Jiang, L., Leblond, P.H., 1992. The coupling of a submarine slide and the surface waves which it generates. J. Geophys. Res. 97, 12,731–12,744.

Jiang, L., Leblond, P.H., 1993. Numerical modeling of an underwater bingham plastic mudslide and the waves which it generates. J. Geophys. Res. 98, 10,303–10,317.

Kelfoun, K., Druitt, T.H., 2005. Numerical modelling of the emplacement of Socompa rock avalanche, Chile. J. Geophys. Res. 110, B12202. doi:10.1029/2005JB003758.

Kelfoun, K., Giachetti, T., Labazuy, P., 2010. Landslide-generated tsunamis at Reunion island. J. Geophys. Res. 115, F04012. doi:10.1029/2009JF001381.

Liu, P.L.-F., Wu, T.-R., Raichlen, F., Synolakis, C.E., Borrero, J.C., 2005. Runup and rundown generated by three-dimensional masses. J. Fluid Mech. 536, 107–144.

Lovholt, F., Pedersen, G., Gisler, G., 2008. Oceanic propagation of a potential tsunami from the la Palma island. J. Geophys. Res. 113, C09026. doi:10.1029/2007JC004603.

Lynett, P., Liu, P.L.-F., 2003. A numerical study of submarine landslide-generated waves and runup. Proc. Roy. Soc. A 458, 2885–2910.

Ma, G., Kirby, J.T., Shi, F., 2013. Numerical simulation of tsunami waves generated by deformable submarine landslides. Ocean Modell. 69, 146–165.

Ma, G., Shi, F., Kirby, J.T., 2012. Shock-capturing non-hydrostatic model for fully dispersive surface wave processes. Ocean Modell. 43-44, 22–35.

Mader, C.L., 2004. Numerical Modeling of Water Waves, 2nd edition CRC press LLC, Boca Raton, Florida.

Mangeney, A., Heinrich, P., Roche, R., 2000. Analytical solution for testing debris avalanche numerical models. Pure Appl. Geophys. 157, 1081–1096.

Masson, D.G., Harbitz, C.B., Wynn, R.B., Pedersen, G., Lovholt, F., 2006. Submarine landslides: processes, triggers and hazard prediction. Phil. Trans. Roy. Soc. A 364, 2009–2039.

Mohammed, F., 2010. Physical modeling of tsunamis generated by three-dimensional deformable granular landslides, Ph.d. dissertation. Georgia Institute of Technology.

Mohammed, F., Fritz, H.M., 2012. Physical modeling of tsunami generated by three-dimensional deformable granular landslides. J. Geophys. Res. 117, C11015. doi:10.1029/2011JC007850.

Montagna, F., Bellotti, G., Di Risio, M., 2011. 3d numerical modeling of landslide-generated tsunamis around a conical island. Nat. Hazards 58, 591–608.

Naranjo, J.A., Arenas, M., Clavero, J., Munoz, O., 2009. Mass movement-induced tsunamis: main effects during the Patagonian Fordland seismic crisis in Aisen (45deg25's), Chile. Andean Geol. 36, 137–145.

Quecedo, M., Pastor, M., Herreros, M.I., 2004. Numerical modelling of impulse wave generated by fast landslides. Int. J. Numer. Meth. Engng 59, 1633–1656.

Savage, S.B., Hutter, K., 1989. The motion of a finite mass of granular material down a rough incline. J. Fluid Mech. 199, 177–215.

Sepulveda, S.A., Serey, A., 2009. Tsunamigenic, earthquake-triggered rock slope failures during the April 21, 2007 Aisen earthquake, southern Chile (45.5°s). Andean Geol. 36, 131–136.

Shi, F., Kirby, J.T., Harris, J.C., Geiman, J.D., Grilli, S.T., 2012. A high-order adaptive time-stepping TVD solver for Boussinesq modeling of breaking waves and coastal inundation. Ocean Mod. 43-44, 36–51.

Skvortsov, A., Bornhold, B., 2007. Numerical simulation of the landslide-generated tsunami in Kitimat Arm, British Columbia, Canada, 27 april 1975. J. Geophys. Res. 112, F02028. doi:10.1029/2006JF000499.

Synolakis, C.E., Bardet, J.-P., Borrero, J.C., Davies, H.L., Okal, E.A., Silver, E.A., Sweet, S., Tappin, D.R., 2002. The slump origin of the 1998 Papua New Guinea tsunami. Proc. R. Soc. A 458, 763–790.

Tappin, D.R., Grilli, S.T., Harris, J.C., Geller, R.J., Masterlark, T., Kirby, J.T., Shi, F., Ma, G., Thingbaijam, K.K.S., Mai, P.M., 2014. Did a submarine landslide contribute to the 2011 Tohoku tsunami? Mar. Geol. 357, 344–361.

Tappin, D.R., Watts, P., McMurtry, G.M., Lafoy, Y., Matsumoto, T., 2001. The Sissano, Papua New Guinea tsunami of July 1998 - offshore evidence on the source mechanism. Mar. Geol. 175, 1–23.

Tappin, D.R., Watts, P., McMurtry, G.M., Lafoy, Y., Matsumoto, T., 2002. Prediction of slump generated tsunamis: the july 17th 1998 Papua New Guinea event. Sci. Tsunami Hazards 20 (4), 222–238.

Toro, E.F., 1997. Riemann Solvers and Numerical Methods for Fluid Dynamics. Springer-Verlag, New York.

Watts, P., Grilli, S.T., Kirby, J.T., Fryer, G.J., Tappin, D.R., 2003. Landslide tsunami case studies using a Boussinesq model and a fully nonlinear tsunami generation model. Nat. Hazards and Earth Syst. Sci. 3, 391–402.

Weiss, R., Fritz, H.M., Wuennemann, K., 2009. Hybrid modeling of the mega-tsunami runup in Lituya bay after half a century. Geophys. Res. Lett. 36, L09602. doi:10.1029/2009GL037814.

Yamazaki, Y., Kowalik, Z., Cheung, K.F., 2009. Depth-integrated, non-hydrostatic model for wave breaking and run-up. Int. J. Num. Meth. Fluids 61, 473–497.

Yuk, D., Yim, S.C., Liu, P.L.-F., 2006. Numerical modeling of submarine mass-movement generated waves using RANS model. Comput. Geosci. 32 (7), 927–935.

Zhou, H., Teng, M.H., 2010. Extended fourth-order depth-integrated model for water waves and currents generated by submarine landslides. J. Eng. Mech. 136 (4), 506–516.